ORIGINAL ARTICLE

Self-propelled nanomotor reconstructs tumor microenvironment through synergistic hypoxia alleviation and glycolysis inhibition for promoted anti-metastasis

Wenqi Yu[a], Ruyi Lin[a], Xueqin He[a], Xiaotong Yang[a], Huilin Zhang[a], Chuan Hu[a], Rui Liu[a], Yuan Huang[a], Yi Qin[b],[*], Huile Gao[a],[*]

[a]Key Laboratory of Drug-Targeting and Drug Delivery System of the Education Ministry and Sichuan Province, Sichuan Engineering Laboratory for Plant-Sourced Drug and Sichuan Research Center for Drug Precision Industrial Technology, West China School of Pharmacy, Sichuan University, Chengdu 610041, China
[b]Department of Orthopedics, Zhuhai Hospital, Jinan University, Zhuhai People's Hospital, Guangdong 519000, China

Abstract   Solid tumors always exhibit local hypoxia, resulting in the high metastasis and inertness to chemotherapy. Reconstruction of hypoxic tumor microenvironment (TME) is considered a potential therapy compared to directly killing tumor cells. However, the insufficient oxygen delivery to deep tumor and the confronting "Warburg effect" compromise the efficacy of hypoxia alleviation. Herein, we construct a cascade enzyme-powered nanomotor (NM-si), which can simultaneously provide sufficient oxygen in deep tumor and inhibit the aerobic glycolysis to potentiate anti-metastasis in chemotherapy. Catalase (Cat) and glucose oxidase (GOx) are co-adsorbed on our previously reported CAuNCs@HA to form self-propelled nanomotor (NM), with hexokinase-2 (HK-2) siRNA further condensed (NM-si). The persistent production of oxygen bubbles from the cascade enzymatic reaction propels NM-si to move forward autonomously and in a controllable direction along H_2O_2 gradient towards deep tumor, with hypoxia successfully alleviated in the meantime. The autonomous movement also facilitates NM-si with lysosome escaping for efficient HK-2 knockdown to inhibit glycolysis. *In vivo* results demonstrated a promising anti-metastasis effect of commercially available albumin-bound paclitaxel (PTX@HSA) after pre-treated with NM-si for TME reconstruction. This cascade enzyme-powered nanomotor provides a

potential prospect in reversing the hypoxic TME and metabolic pathway for reinforced anti-metastasis of chemotherapy.

1. Introduction

Triple negative breast cancer (TNBC) is an aggressive disease with high mortality among women in the world[1]. The high metastasis rate of TNBC always result in poor prognosis and therefore compromise the efficacy of conventional chemotherapy[2]. Increasing evidence showed that the special hypoxic tumor microenvironment (TME) was strongly responsible for the increased metastasis[3]. By regulating the metabolism pathway[4], promoting the stemness of cancer stem cells[5,6], and inducing immune suppressive microenvironment[7,8], the low oxygen tension comprehensively promotes the aggressiveness of TNBC from diverse aspects[9]. Just as soil is to seeds, modulation of TME can affect the occurrence and development of tumors in an all-round way when comparing to directly killing tumor cells, which is therefore considered a very potential therapeutic method in recent years. However, the alleviation of hypoxic TME still faces several challenges that makes the effect of hypoxia attenuation not satisfactory. As is known, tumor site always exhibits dense extracellular matrix (ECM) and tortuous blood vessels, which restricts the oxygen carriers around the blood vessels but cannot penetrate deeply in tumor[10,11], while hypoxia is exactly present at deep tumor region. Another problem is the insufficient generation of oxygen. Although the commonly used oxygen carriers such as perfluorochemicals and hemoglobin can adsorb oxygen and appropriately deliver to tumor site, the content of delivered oxygen is very limited with only one dosage but cannot provide a repeated supplement for a long-term hypoxia alleviation[12-14]. Therefore, it's an urgent need to alleviate tumor hypoxia with efficient oxygen delivery and sufficient oxygen generation.

Recently, nanomotors represent as emerging novel nanomaterials for drug delivery[15,16]. Different from traditional nanodrugs which passively flow with blood during the circulation process, nanomotors can convert the surrounding energies into mechanical forces, which breaks the shackles of irregular Brownian motion and exhibits an autonomous movement[17]. Moreover, the direction of the locomotion trajectory can be manipulated by external field (ultrasound and magnetic field), or move directionally towards the chemoattractant gradient[18-20]. Therefore, we deem that nanomotor with self-propelled motion behavior is an ideal carrier to deliver oxygen to deep tumor where is previously inaccessible for other nanoparticles. As the concentration of hydrogen peroxide (H_2O_2) is specifically much higher in tumor site than normal tissues[21], we chose the endogenous H_2O_2 as fuel and catalase (Cat) as catalyst to gain the driving force in tumor site. In the meantime, oxygen bubbles could be persistently generated during the enzymatic reaction with hypoxia together alleviated, which is a "two-birds-one-stone" strategy. To also gain autonomous movement during blood circulation, we adopted glucose oxidase (GOx) together with Cat to construct a cascade enzymatic reaction. H_2O_2 is produced along with the consumption of glucose and is quickly scavenged by Cat for propelling without doing any harm to normal tissues [Eqs. (1) and (2)]. Moreover, as tumor cells are more sensitive to the fluctuation of glucose level, GOx synergistically exerts starvation therapy for anti-tumor treatment.

$$\text{Glucose} + O_2 + H_2O \overset{\text{GOx}}{\rightarrow} H_2O_2 + \text{Gluconic acid} \qquad (1)$$

$$H_2O_2 \overset{\text{Cat}}{\rightarrow} H_2O + O_2 \qquad (2)$$

However, only reversing the oxygen level is far from enough. More and more studies found that tumor cells still preferred glycolysis pathway instead of oxidative phosphorylation when transferred back to normoxia environment, which is called aerobic glycolysis, also known as "Warburg effect"[22]. And lactic acid, the product of glycolysis, further promotes the endothelial-to-mesenchymal transition (EMT), activates tumor cell detachment and degrades ECM[23,24], which therefore compromises the anti-metastasis effect of hypoxia alleviation. As a result, combination therapy of glycolysis inhibition is necessary along with hypoxia amelioration, while there is rarely reported yet. Hexokinase-2 (HK-2) is the key rate limiting enzyme during the aerobic glycolysis process and is specifically up-regulated in tumor[25,26]. Due to the special way of piercing into cells facilitates nanomotors with lysosome escaping[27], we co-delivered small interfering RNA (siRNA) to knockdown the expression of HK-2 and therefore inhibiting aerobic glycolysis. In addition, as HK-2 plays a role in the first step of glucose utilization, the downregulation also cuts off the glucose resource to starve cancer cells.

Altogether, the cascade enzyme-powered nanomotor was constructed to modulate the hypoxic TME along with the glycolysis inhibition to prevent TNBC metastasis. GOx and Cat were co-adsorbed on our previously reported cationic gold nanoclusters (CAuNCs@HA) to form self-propelled nanomotor (NM)[28], with HK-2 siRNA further condensed (NM-si). Oxygen bubbles could be persistently generated from the cascade enzymatic reaction, facilitating NM with a faster self-propelling autonomous movement and deeper tumor penetration. Also, the H_2O_2-fueled NM exhibited a chemotaxis nature toward the H_2O_2 gradient from blood circulation along to the tumor site, showing not only autonomous but also a directional movement. Accompanied with the self-powered movement to deep tumor, the persistently generated oxygen bubbles ameliorated the hypoxia condition to reconstruct TME. Knockdown of HK-2 inhibited the process of aerobic glycolysis and synergistically functioned well with hypoxia alleviation. The inhibition of metastasis was evaluated with commercially available albumin-bound paclitaxel (PTX@HSA), and the lung metastasis of TNBC was significantly inhibited when pre-treated with NM-si. Therefore, the proposed cascade enzyme-powered nanomotor is a promising nanoplatform for reversing the hypoxic TME and metabolic pathway, paving road for the anti-metastasis of TNBC in chemotherapy (Fig. 1).
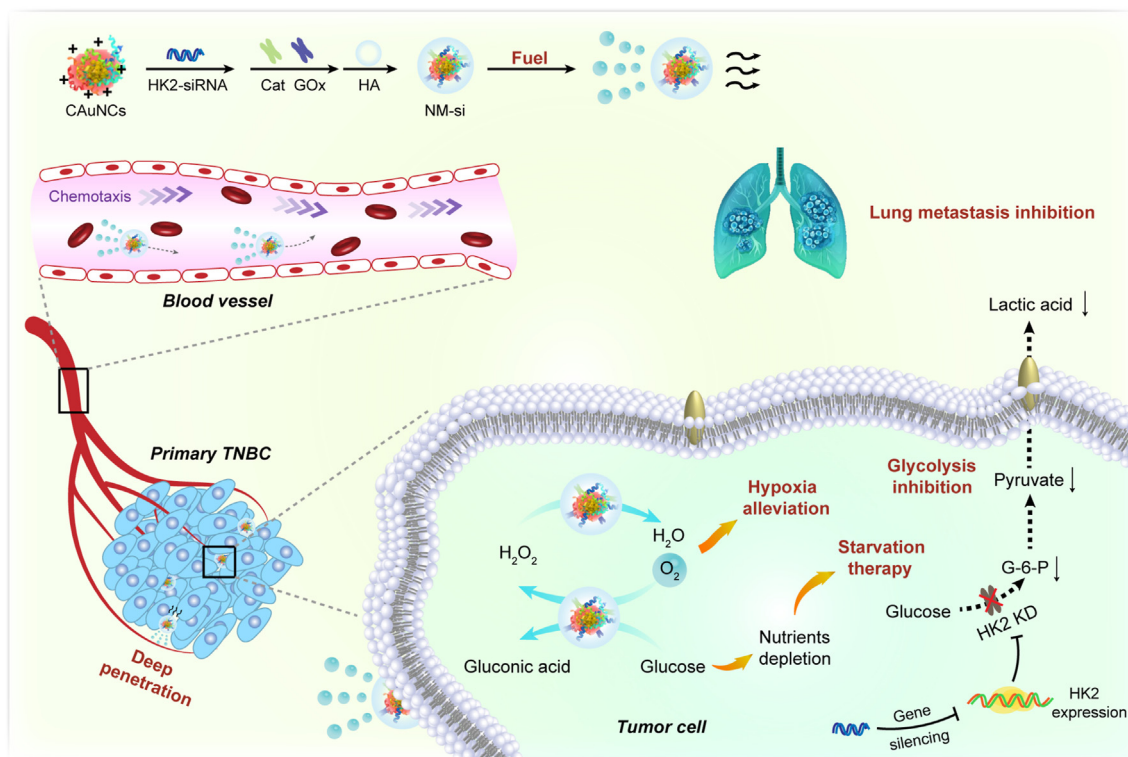
Figure 1 Schematic illustration of the cascade enzyme-powered nanomotor (NM-si) for TME modulation. The NM-si moves autonomously in blood circulation towards primary TNBC, and generates oxygen in deep tumor for hypoxia alleviation. Along with the glycolysis inhibition and starvation therapy, TNBC and lung metastasis are significantly inhibited.

2. Materials and methods

2.1. Materials

Chloroauric acid (HAuCl$_4$·3H$_2$O), Glucose oxidase (G6125), Catalase (C1345), rat tail collagen I (C3867) and bovine serum albumin (BSA, MW = 66 kDa) were purchased from Sigma Aldrich (Shanghai, China), Hyaluronic acid (MW = 68 kDa) was obtained from Freda Biopharm Co., Ltd. (Shandong, China). siRNA (HK-2, NC and HK-2-FAM) were synthesized by Gene Pharma Co., Ltd. (Shanghai, China). The sequence of HK-2 was 5′-GAUCCGCAGACGUGUAAAUdTdT-3′ (sense) and 5′-AUUUACACGUCUGCGGAUCdTdT-3′ (antisense). FAM was labeled at the 5′ end of siRNA. Primer sequence of *HK-2*: Forward: ATGATCGCCTGCTTATTCACG and Reverse: CGCCTAGAAATCTCCAGAAGGG; and β-actin Forward: GTGACGTTGACATCCGTAAAGA and Reverse: GCCGGACTCATCGTACTCC. Real Time PCR Easy-SYBR Green I kit was purchased from Foregene (Chengdu, China). Crystal violet was purchased from Solarbio Science & Technology Co., Ltd. (Beijing, China). Anti-Hexokinase 2 (ab209847) and anti-HIF-1α (ab179483) were purchased from Abcam Co., Ltd. (Cambridge, UK). Hypoxyprobe™-1 Omni Kit was purchased from Hypoxyprobe, Inc. (Burlington, USA). Anti-CD31 (GB11063-3) was purchased from Servicebio Co., Ltd. (Wuhan, China). Female BALB/c-nude and BALB/c mice were purchased from Ensiweier Biotechnology Co., Ltd. (Chongqing, China). All animal experiments were performed under the guidelines evaluated and approved by the ethics committee of Sichuan University.

2.2. Binding affinity of CAuNCs

The CAuNCs-siRNA at various mass ratios (0, 0.5, 2.5, 5, 10, 25, 50, and 100) containing 1 μg of HK-2 siRNA per well was loaded with loading buffer in a Gelred-stained agarose gel (2%). Electrophoresis was carried out at 100 V for 30 min in Tris-Acetate-EDTA (TAE) buffer. Then the gel was visualized under UV irradiation mode by a bioimage system (Bio-Rad, Chemidoc XRS+, USA).

2.3. Preparation and characterization of enzyme-powered nanomotor (NM-si)

The cationic gold nanoclusters (CAuNCs) were synthesized according to our previous work[28]. Then, 30 μL siRNA (20 μmol/L in DEPC water) was added to 200 μL CAuNCs (2 mg/mL) and vortex for several minutes to give a fully condensation of siRNA. To form NM-si, GOx (100 μg/mL, 40 μL), Cat (100 μg/mL, 26.67 μL) and HA (0.67 mg/mL, 200 μL) were added sequentially and vortex for 2 min. Size and zeta potential of NM-si were measured by dynamic light scattering (DLS) analysis (Zetasizer Nano ZS, Malvern, UK). And TEM (H-600, Hitachi, Japan) at 75 kV was used to study the morphological characteristics of NM-si.

2.4. Motion behavior of NM

The motion behavior of NM was observed through an inverted epifluorescence microscope (Nikon, Ti-E, Japan) by NTA (nanoparticle tracking analysis) method. Briefly, an aqueous solution of NM was mixed with different substrates (distilled water, H$_2$O$_2$, glucose, and H$_2$O$_2$ + glucose) and then transferred to microwells

immediately (final concentration: 100 μmol/L H_2O_2, 5 mmol/L glucose, 1 mg/mL NM). The motion of NM was captured at 30 fps and videos of 30 s were recorded up to the first 3 min. The tracking trajectories of NM under different substrates could be drawn with the x and y positional data extracted from the recording video *via* NIS Elements 4.0 software. Mean-squared displacement (MSD) and diffusion coefficient (D_e) was calculated using the following Eqs. (3) and (4)

$$MSD(\Delta t) = \langle (x_i(t + \Delta t) - x_i(t))^2 \rangle (i = 2, \text{ for 2D analysis}) \quad (3)$$

$$MSD(\Delta t) = 4D_e \Delta t + v^2 \Delta t^2 \quad (4)$$

2.5. Rat tail collagen penetration experiment

Rat tail collagen I (141.75 μL, 4.5 mg/mL) was gently mixed with sodium hydroxide aqueous (3.8 μL, 1 mol/L) and EDTA-2Na aqueous (19.5 μL, 0.17 mol/L), and then added into microslide capillary tubes (Cat. 63843-05, emsdiasum, USA). After incubation in 37 °C overnight, NM with different substrates were mixed and added from the left end of the capillary tube (final concentration: 100 μmol/L H_2O_2, 5 mmol/L glucose and 0.5 mg/mL NM). The microslide tubes were observed 40 min later under confocal microscope to determine the movement distance. For chemotaxis analysis, substrates were added from the right end of capillary tubes instead, with NM still added from the left end.

2.6. In vivo biodistribution

Female BALB/c nude mice ($\sim$20 g, $n = 5$) were orthotopically implanted with 4T1 cells at a density of 5×10^5 into the second breast pad on the left side. Then nanoparticles were intravenously injected with CAuNCs-GOx@HA, CAuNCs-Cat@HA and NM, respectively at a dosage of 1 mg BSA each. Major organs and tumors were collected and imaged by Lumina III Imaging System (Perkin Elmer, USA). And the fluorescence intensities were semi-quantified for comparison. Further, tissues were sliced and stained with DAPI, the fluorescence of nanoparticles were observed through confocal microscope (Nikon, A1R+, Japan).

2.7. Wound healing

4T1 cells were seeded in 12-well plates and incubated until 90% confluency. Subsequently, the scratched wounds were generated with a 200-μL pipette tip and debris was removed by washing twice with PBS. Then, serum-free medium with different nanoparticles (final concentration: AuNCs, 2 μg/mL; H_2O_2, 2 μmol/L) were added and incubated for another 24 h in hypoxic environment. Images were taken at 0 and 24 h under a microscope (Olympus, BX60, Japan), and the areas of wounds were semi-quantified by Image J 6.0 software (NIH, USA).

2.8. In vitro invasion

For invasion assay, 4T1 cells were firstly starved in RPMI 1640 medium (without serum) for 12 h before seeded into the upper chambers of transwells (24-well; pore size: 8 μm; Corning, USA) with a density of 3×10^5 (Transwells were precoated with Matrigel, 25 μg/well, BD Bioscience). Then, another 100 μL of nanoparticles (final concentration: AuNCs, 2 μg/mL; H_2O_2, 2 μmol/L) in serum-free medium were added to each upper

chamber, while the lower chambers were filled with 600 μL RPMI 1640 medium containing 20% FBS as chemoattractant. After incubation in hypoxic environment for 24 h, cells were fixed with 4% paraformaldehyde and stained with crystal violet for 20 min. Cells in the upper chambers were removed by a cotton swab, and the invaded cells to the lower side of membrane were imaged by an inverted microscope. For further quantitative measurement, the crystal violet was dissolved in 33% acetic acid, and the absorbance was detected at 570 nm by microplate reader (Thermo Scientific, Varioskan Flash, USA).

2.9. Effect of siRNA interference on migration and invasion in vitro

4T1 cells were seeded in 10-cm petri dishes and cultured in RPMI 1640 medium (without antibiotics) till 40% confluency. Subsequently, NM and NM-si (2 μg siRNA) were incubated with cells for 5 h and then replaced with complete medium. After 48 h, cells were collected and counted. For migration assay, cells were seeded in the upper chambers of transwells at a density of 1×10^5, and then lower chambers were placed with RPMI 1640 medium containing 20% FBS as chemoattractant. After incubated for another 24 h, cells that did not migrate through the Transwell membrane were removed by a cotton swab, and the remaining cells were fixed and stained with crystal violet for further observation and quantitative measurement. The invasion assay was the same as the migration assay, except that the upper chambers were pre-coated with Matrigel before cells (3×10^5 per chamber) were seeded.

2.10. In vivo microenvironment modulation

Female BALB/c mice were orthotopically implanted with 4T1 cells at a density of 5×10^5 into the second breast pad on the left side. Then nanoparticles (CAuNCs-GOx@HA, CAuNCs-Cat@HA, NM, NM-si) were intravenously injected on Days 8, 11 and 15 at a dosage of 1 mg BSA of CAuNCs each (measured by BCA assay). On Day 20, mice were intraperitoneal injected with 60 mg/kg of pimonidazole (Hypoxyprobe™-1) at 1 h before being sacrificed. Then major organs and tumors were collected for further experiments. To evaluate the hypoxia microenvironment, tumor slices were stained with anti-pimonidazole antibody and anti-CD31 antibody, the hypoxia region and tumor blood vessels were observed under confocal microscope. Moreover, total protein was extracted from tumor to further detect the expression of HIF-1α. The inhibition of aerobic glycolysis was detected by measuring the expression of HK-2 protein.

2.11. In vivo anti-tumor and anti-metastasis effect

Female BALB/c mice were orthotopically implanted with 4T1 cells at a density of 5×10^5 into the second breast pad on the left side. NM-si was intravenously given on Days 8, 11 and 15, and PTX@HSA (NM-si: 50 mg/kg, PTX: 5 mg/kg) were given the next day after NM-si. The tumor volume and body weight were recorded every two days and mice were then sacrificed on Day 20. Major organs and tumors were collected for H&E and TUNEL staining and microenvironment modulation evaluation. To evaluate the anti-metastasis effect, *ex vivo* lungs were stained and fixed with Bouin's liquid to count the metastasis nodules. The metastasis nodules were divided into four grades: grade I < 0.5 mm; 0.5 mm $\leq$ grade II < 1 mm; 1 mm $\leq$ grade III < 2 mm; grade IV > 2 mm. Number of metastasis nodules were calculated as I $\times$ 1 + II $\times$ 2 + II $\times$ 3 + IV $\times$ 4.
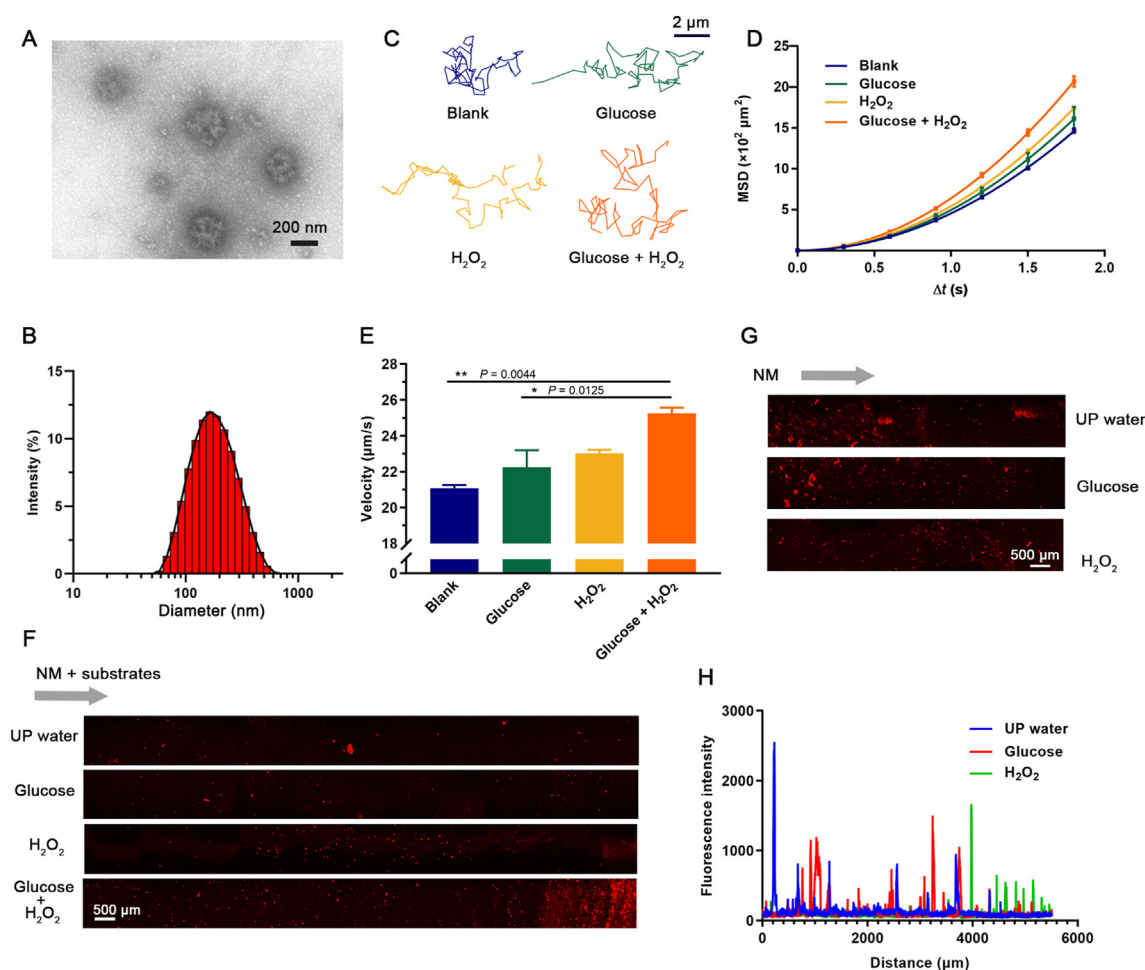
Figure 2 (A) TEM image and (B) DLS detection of NM. (C) Track trajectories of NM under different substrates at the time lapse of 2.7 s. Scale bar = 2 μm. (D) Mean squared displacement (MSD) and (E) velocity analysis of NM under different substrates. Data are presented as mean ± SD (n = 3), and one-way ANOVA with Tukey multiple comparisons post-test was used for (E); *$P < 0.05$, **$P < 0.01$. (F) Rat tail collagen diffusion of NM under different substrates. (G) Chemotaxis of NM demonstrated by rat tail collagen diffusion with NM on one side and chemoattractant on the other side. (H) Quantitative analysis of fluorescence intensity along with distance in (G).

2.12. Statistical analysis

All data are presented as mean ± standard deviation (SD). Un-paired Student's t-test was used for comparison of two groups. One-way ANOVA with Tukey multiple comparisons post-test was used for multi-group analysis. Two-way ANOVA with Tukey multiple comparisons post-test was used for two-factors multi-group analysis.

3. Results and discussion

3.1. Preparation and characterization of NM

To construct the self-powered NM, we used cationic gold nano-clusters (CAuNCs) to adsorb cascade enzymes due to their high positive charge. The synthesis of CAuNCs has been reported pre-viously by our group[28,29]. GOx and Cat could be easily adsorbed on CAuNCs *via* electrostatic interactions. As the cationic nano-particles were reported to have great toxicity to body and were easily excreted[30,31], we further non-covalently coated negatively charged hyaluronic acid (HA) on CAuNCs to balance the charge and endowed with active tumor targeting at the same time[32].

Dynamic light scanning (DLS) results showed that the synthesized NM exhibited a narrow polydispersity with an average particle size of 171.53 ± 1.40 nm, and possessed a negative zeta potential of −26.0 ± 0.47 mV (Fig. 2A and Supporting Information Table S1). Transmission electron microscopy (TEM) indicated the spherical morphology of NM and revealed the same size as DLS (Fig. 2B). To further detect the amount of enzymes adsorbed on CAuNCs, we attached fluorescent molecules FITC to GOx and Cat, respectively. The encapsulation efficiency and drug loading capacity of GOx were 93.7 ± 2.8% and 0.92 ± 0.03%, respectively, and 99.0 ± 0.1% and 0.65 ± 0.01%, respectively of Cat.

3.2. Motion behavior of NM

To evaluate whether NM with cascade enzymes of GOx and Cat could move autonomously under the intrinsic glucose or H_2O_2, the track trajectories under different substrates were recorded for 2.7 s by optical tracking (Fig. 2C). Also, the x–y coordinates from the optical tracking were extracted for the mean squared displacement (MSD) calculation according to Eq. (3) (Fig. 2D). It was shown that with the existence of both glucose and H_2O_2, NM exhibited the most extended trajectory comparing with other groups, which

may due to the sufficient H_2O_2 provided by both the oxidation product of glucose and the aqueous substrate solution. Different from the random Brownian motion in blank group, the path of NM was propelled directionally in glucose and H_2O_2 group. This special movement might result from the constant pinning of oxygen bubbles, which not only speeded up the motion, but also pushed NM forward. Notably, the motion in glucose solution was slightly slower than H_2O_2 group, which was because of the time lag that glucose oxidation reaction needed for H_2O_2 production. Subsequently, we fitted the MSD−Δt line with Eq. (4),[33] and obtained the average velocity of NM (Fig. 2E). As shown, the average velocity of NM without any substrates was only 21.09 ± 0.17 μm/s, while the speed increased after adding substrates. And it increased to 25.25 ± 0.33 μm/s under the existence of both glucose and H_2O_2. There was significant difference between the glucose + H_2O_2 group and other two groups (blank and glucose), which further proved the pivotal role of instant oxygen production in motion propelling.

3.3. Penetration and chemotaxis of NM

In solid tumors, the dense interstitial ECM impedes the penetration of nanodrugs, which constrains the delivery of nanodrugs only around the blood vessels but cannot reach to tumor parenchyma. Here, we detected whether the autonomous movement of nanomotor could exert better ECM penetration ability, and carried drugs to deep tumor. Rat tail collagen was used to simulate interstitial matrix, and NM mixed with different substrates were added at the left side of capillary tubes (Fig. 2F). It was shown that, after 1 h, the majority of NM with glucose + H_2O_2 almost moved to the right end of the capillary tube, while NM under ultrapure water (UP water) randomly scattered at the beginning, suggesting a faster and deeper penetration behavior of NM after gaining self-propelling force. Usually, nanomotors using H_2O_2 as fuel always exhibit chemotaxis characteristic toward H_2O_2 gradient[34,35], which is very similar to chemokine-dependent immune cells recruitment from immune organs to tumor site. As the concentration of H_2O_2 is much higher in tumor than normal tissues, we further tested whether the cascade enzyme-formed NM also have the chemotaxis toward H_2O_2, which could guide NM to move directionally toward tumor from circulating blood. The rat tail collagen in capillary tube was also used as a model. Differently, UP water, glucose and H_2O_2 were added at the right end of tubes with NM added at the left end. It suggested that NM showed significant chemotaxis toward H_2O_2 with the farthest distance (Fig. 2G and H).

3.4. Catalytic activity of NM

After successfully loading GOx and Cat in NM, we then detected the catalytic property of NM to ensure the enzyme activities still remained. The free GOx was used as positive control. In normoxic condition, the depletions of glucose were observed both in GOx and NM group (Fig. 3A), and it revealed that NM could even accelerate glucose consumption, which may because of the constant oxygen produced by the cascade enzymatic reaction. The change in pH indicated the same results (Fig. 3B). The pH value of glucose solutions remained stable at around 6.25. However, a dramatic pH drop was detected after treatment with NM, from 6.18 to 3.53 in only 6 h. In hypoxic condition, H_2O_2 was added as comparison to evaluate whether the endogenous H_2O_2 in tumor sites could further improved the catalytic efficacy (Fig. 3C and D).

As shown, the hypoxic microenvironment slowed down the enzymatic reaction to some extent due to the lack of oxygen for glucose oxidation. However, with the addition of H_2O_2, the restrain of oxygen could be alleviated. By producing oxygen through Cat catalysis priorly, the depletion of glucose in hypoxia was promoted compared with NM without the existence of H_2O_2. Even though the catalytic rate of NM + H_2O_2 under hypoxia was not as high as NM under normoxia, it still exhibited higher glucose depletion and pH decrease compared with free GOx. To further detect whether the cascade catalytic reaction could relief hypoxia, we tested the dissolved oxygen during the time after adding different preparations (Fig. 3E and F). In normoxia, NM exhibited a slower O_2 decrease than free GOx; and in hypoxia, there was an instant O_2 increase of NM + H_2O_2, with the dissolved oxygen increased from 1.98 to 3.70 mg/L in only 0.5 h, and further increased to 5.96 mg/L in 1 h, which was approaching the concentration of oxygen in normoxia (8 mg/L).

Encouraged by the excellent catalytic activity, the effectiveness of NM for glucose consumption and hypoxia alleviation were further evaluated on cellular level (Fig. 3G). There was a dramatic drop of glucose concentration from the beginning of 16.6 to almost 5 mmol/L after 24 h whether with H_2O_2 or not. Notably, even though the consumption of glucose in NM + H_2O_2 group was little bit faster than NM in the first 10 h, there was no differences between these two groups in the long period of time (24 h). Immunofluorescence assay was used to examine the level of hypoxia inducible factor-1α (HIF-1α), a hallmark of hypoxia (Fig. 3H). Under hypoxia condition, the PBS group exhibited strong fluorescence of HIF-1α, and there was a tendency that HIF-1α translocated to nuclei, which was the characteristic response of cells under hypoxia. In contrast, NM group showed a much weaker fluorescence and HIF-1α mainly located in cytoplasm, demonstrating the relief of hypoxia. Moreover, when incubated together with H_2O_2, NM displayed better ability for hypoxia alleviation. In the confocal laser scanning microscope (CLSM) results, we also noticed that the hypoxia was slightly relieved with only Cat (CAuNCs-Cat@HA), which might because the tumor cells themselves could produce H_2O_2 at a rate of 0.5 nmol/10^4 cells/h[21].

3.5. Cellular uptake of NM

As the NM exhibited promoted motion behavior in aqueous solution, we further explored whether the special movement had a positive effect on cellular uptake. Flow cytometry results indicated that the promoted velocity indeed speeded up the cellular uptake (Fig. 4A). Compared with 4T1 cells treated with only GOx (CAuNCs-GOx@HA), there was a significant enhanced fluorescence intensity after treatment with NM at 1 and 2 h. Moreover, CAuNCs-Cat@HA group also displayed an accelerated uptake than CAuNCs-GOx@HA group, which might because of the oxygen bubbles generated through the catalysis of endogenous H_2O_2, which was coordinated with the HIF-1α immunofluorescence assay. Notably, there was no significant difference among the three groups at 4 h, indicating that the increased speed of NM only worked in a relatively short time for promoting the cellular uptake, while it did not affect the cellular uptake and accumulation in the long period of time. The confocal results also displayed the same trend (Fig. 4B).

3.6. In vivo biodistribution

Encouraged by the excellent autonomous movement in cellular experiment, we further investigated the biodistribution of NM
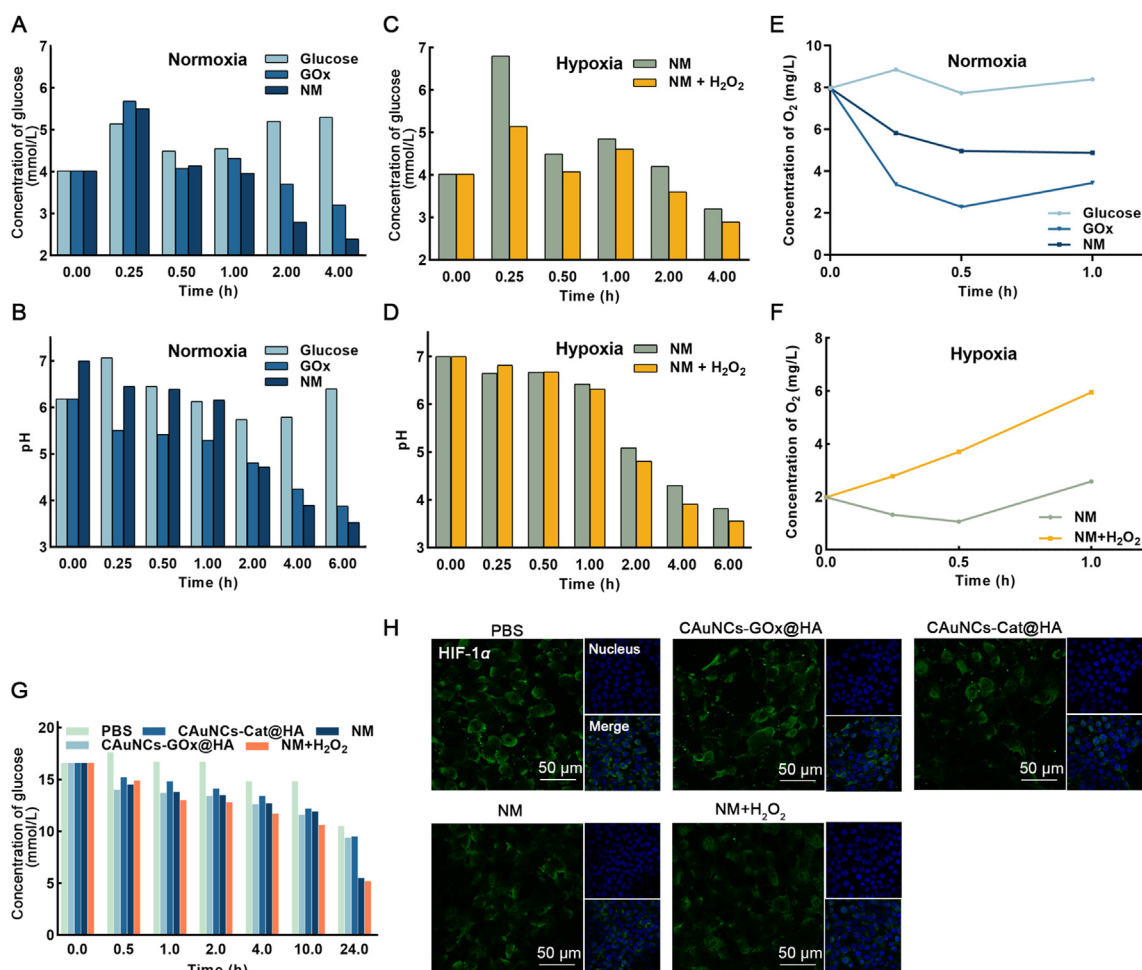
Figure 3 (A) Concentration of glucose with time after different treatments under normoxia and (C) hypoxia condition. (B) pH value changes with time of glucose solution after different treatments under normoxia and (D) hypoxia condition. (E) The dissolved oxygen concentration changes of glucose solution after different treatments under normoxia and (F) hypoxia condition. (G) Glucose concentration changes of culture medium after 4T1 cells were treated with different nanoparticles. (H) Hypoxia level of 4T1 cells after different treatments, and the hypoxia was reflected *via* immunofluorescence images of HIF-1α. Blue represents nucleus, and green represents HIF-1α. Scale bar = 50 μm.

in vivo by IVIS living system. 4T1 tumor-bearing mice were intravenously injected with different formulations and then imaged at various time points (Supporting Information Fig. S1). Obvious fluorescence was detected early at 2 h post injection, and NM group showed the strongest fluorescence intensity at tumor site. As time extended, the fluorescence intensity of NM at tumor site reached to a peak at 6 h and then decreased. Mice were then sacrificed for *ex vivo* analysis 8 h post injection. As shown, the NM group exhibited the strongest fluorescence intensity at tumor site even after 8 h, and the semi-quantitative analysis revealed that there was a significant difference of tumor accumulation between NM and CAuNCs-GOx@HA (Fig. 4C and D, and Supporting Information Fig. S2), illustrating a faster movement of NM to tumor. Remarkably, tumors resected from CAuNCs-Cat@HA group exhibited a relatively stronger fluorescence intensity compared with CAuNCs-GOx@HA group, which might due to the obtained chemotactic self-driven force with the increased concentration of endogenous H_2O_2 in tumor site. Additionally, frozen slices (Fig. 4E and Supporting Information Fig. S3) showed that NM exhibited strong fluorescence both in margin and center area of tumor. Further demonstrated that the autonomous movement

facilitated NM to get into tumors not only with a faster speed but also with deeper penetration behavior *in vivo*.

3.7. siRNA delivery

Nanomotors were reported to exhibit a unique way of entering into cells that they pierced and travelled inside the cells through the self-propelling rather than other common ways like the membrane fusion or the receptor-mediated endocytosis, which is a good vector for gene delivery without getting trapped in lysosome[36]. Therefore, we further condensed HK-2 siRNA on NM to inhibit the aerobic glycolysis and synergistically work with hypoxia alleviation. Firstly, the binding affinity of CAuNCs at various mass ratios (0, 0.5, 2.5, 5, 10, 25, 50, and 100) was evaluated by electrophoresis (Fig. 5A). Results demonstrate that with the ratio increased, there were less unbound siRNA. And when the mass ratio of CAuNCs and siRNA was 50 or higher, there was no free siRNA, suggesting the optimal binding ratio. Considering that the stronger electrostatic attraction between siRNA and vehicles at higher *N/P* ratios would suppress the release of siRNA[37], we chose 50:1 (*w/w*) as the final condensation ratio.
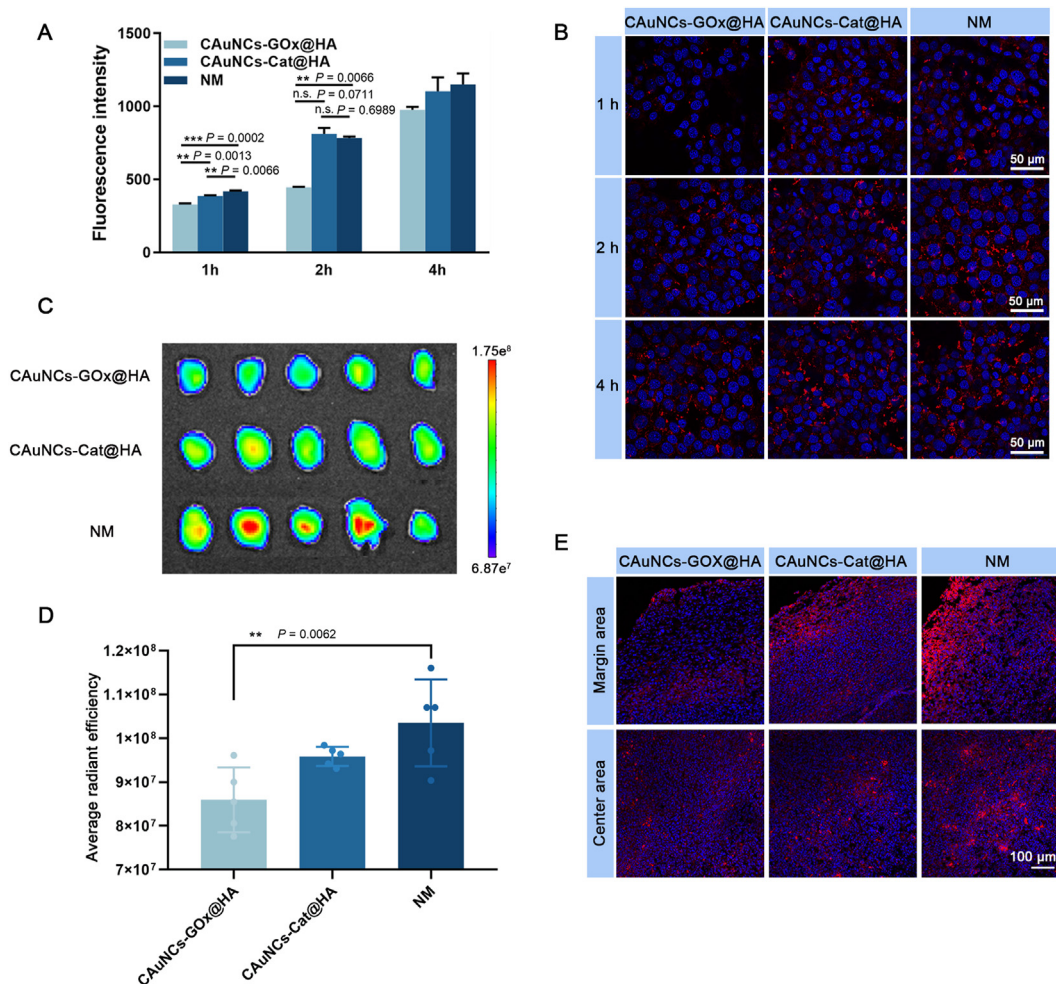
Figure 4 (A) Quantitative and (B) qualitative cellular uptake of 4T1 cells. In the confocal images, blue represents nucleus, and red represents nanoparticles. Scale bar = 50 μm. Data are presented as mean ± SD (n = 3), and two-way ANOVA with Tukey multiple comparisons post-test was used for (A); **$P < 0.01$, ***$P < 0.001$, n.s., not significant. (C) *Ex vivo* imaging of tumors at 8 h post injection and (D) their semi-quantification analysis. Data are presented as mean ± SD (n = 5), and one-way ANOVA with Tukey multiple comparisons post-test was used for analysis; **$P < 0.01$. (E) Confocal images of frozen tumor slices at 8 h post injection. Blue represents nucleus, and red represents nanoparticles. Scale bar = 100 μm.

The intracellular uptake and distribution of NM-si were evaluated through CLSM at the optimum ratio. As shown, siRNA distributed throughout the cytosol and there was no co-localization between siRNA and lysosomes during the whole uptake period from 1 to 4 h (Fig. 5E). The intensity profile and Pearson's correlation coefficient (Rr) of the CLSM results were further analyzed to quantitatively clarify the colocalization between siRNA and lysosome (Fig. 5E and Supporting Information Fig. S4). Generally, it is considered to have colocalization when Rr is greater than 0.6. While in our results, the calculated Rr was much less than 0.6, with only 0.08, 0.13 and 0.25 at 1, 2 and 4 h, respectively, indicating the nanomotor-delivered siRNA were not entrapped by lysosomes. Intensity profile illustrated the same results that there was no overlapping peak between siRNA-FAM and Lyso Red. This behavior of NM protected siRNA from decomposition by the lysosomal hydrolases and could promote siRNA interference efficiency. Moreover, the fluorescence of siRNA in 4T1 cells was significantly enhanced with time, demonstrating that NM-si displayed a time-dependent internalization manner.

Due to the exciting results of siRNA delivery, we further detected the RNA interference efficiency in 4T1 cells. After treatment with NM-si for 5 h, the total RNA and protein of 4T1 cells were extracted after culturing for another 48 and 72 h, respectively. Results showed that there was an 32% knockdown of *HK-2* expression in 4T1 cells when compared to PBS group (Fig. 5B–D). NM itself and NM loaded with disordered RNA sequence (NM-NC) was set as control group, and almost no decreased expression of *HK-2* was observed, which further verified the successful delivery of *HK-2* siRNA (Supporting Information Fig. S5).

3.8. In vitro cytotoxicity

To investigate the starvation therapy efficacy caused by glucose depletion, we detected the cytotoxicity of NM-si against 4T1 cells *in vitro*. As shown in MTT result, CAuNCs@HA and CAuNCs-Cat@HA exhibited low inhibition rates with less than 50% in terms of a concentration range up to 22.22 μg/mL. While once encapsulated with GOx, the viability rate of 4T1 cells displayed a sharp drop (Fig. 5F). We further calculated the half maximal inhibitory concentration (IC$_{50}$), which made the inhibition more intuitive. It turned out that the IC$_{50}$ of CAuNCs@HA and
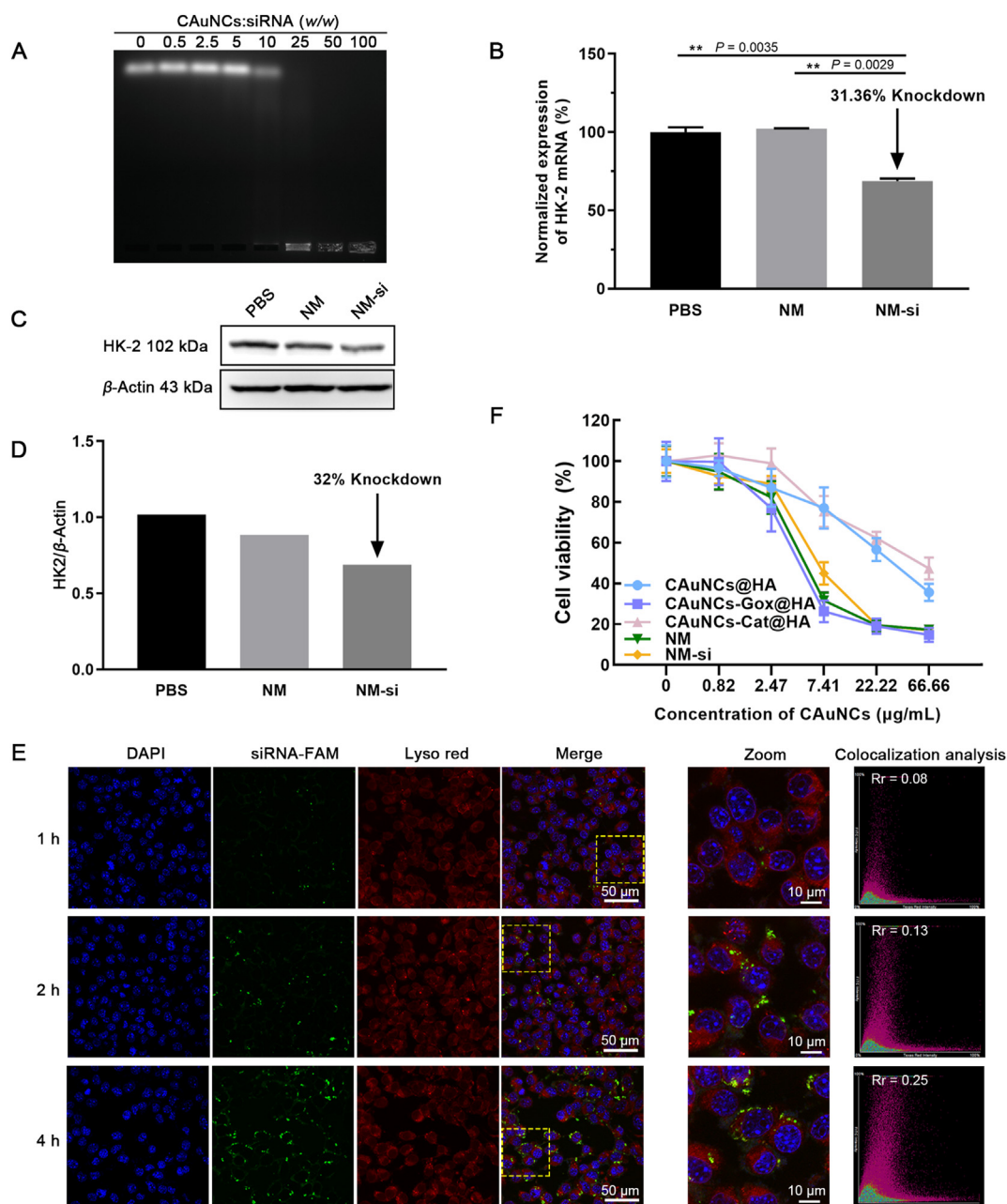
Figure 5 (A) Binding affinity of HK-2 siRNA to CAuNCs under different mass ratio detected through agarose gel electrophoresis. (B) Normalized expression of HK-2 mRNA detected by qRT-PCR. One-way ANOVA with Tukey multiple comparisons post-test was used; **$P < 0.01$. (C) Western blot analysis of HK-2 expression in 4T1 cells to evaluate the RNA interference effect. (D) Semi-quantitative analysis of western blot by Image J. (E) Confocal images of 4T1 cells at different time points after treated with NM-siRNA-FAM. Blue represents nucleus, green represents siRNA, and red represents lysosome. Scale bar = 50 μm. Zoom scale bar = 10 μm. The colocalization between siRNA and lysosome was calculated through NIS-Elements Viewer 4.2. (F) *In vitro* cytotoxicity of 4T1 cells after treated with different nanoparticles.

CAuNCs-Cat@HA was 31.47 and 47.07 μg/mL, respectively, while the value decreased dramatically to only 6.33, 7.02 and 8.68 μg/mL for CAuNCs-GOx@HA, NM and NM-si, respectively, demonstrating the severe 4T1 cell eradication capacity of GOx. We also noticed that, even though HK-2 acted as a rate-limiting enzyme in the process of glycolysis, which could also affect the utilization of glucose in some way, the cytotoxicity displayed in the MTT assay was not that obvious when comparing between NM and NM-si. We deduced that 24 h, which was the most common time period for MTT assay, was not enough for

siRNA interference and therefore compromised the inhibition rate. The function of *HK-2* silencing would emerge in the longer time.

3.9. *In vitro* inhibition of cell migration and invasion

The hypoxia microenvironment and aerobic glycolysis were reported to be related with tumor metastasis[3,4]. Here, we evaluated whether the relief of hypoxia or the inhibition of aerobic glycolysis after treatment with NM could suppress the metastasis. We firstly investigated the migration ability of 4T1 cells through
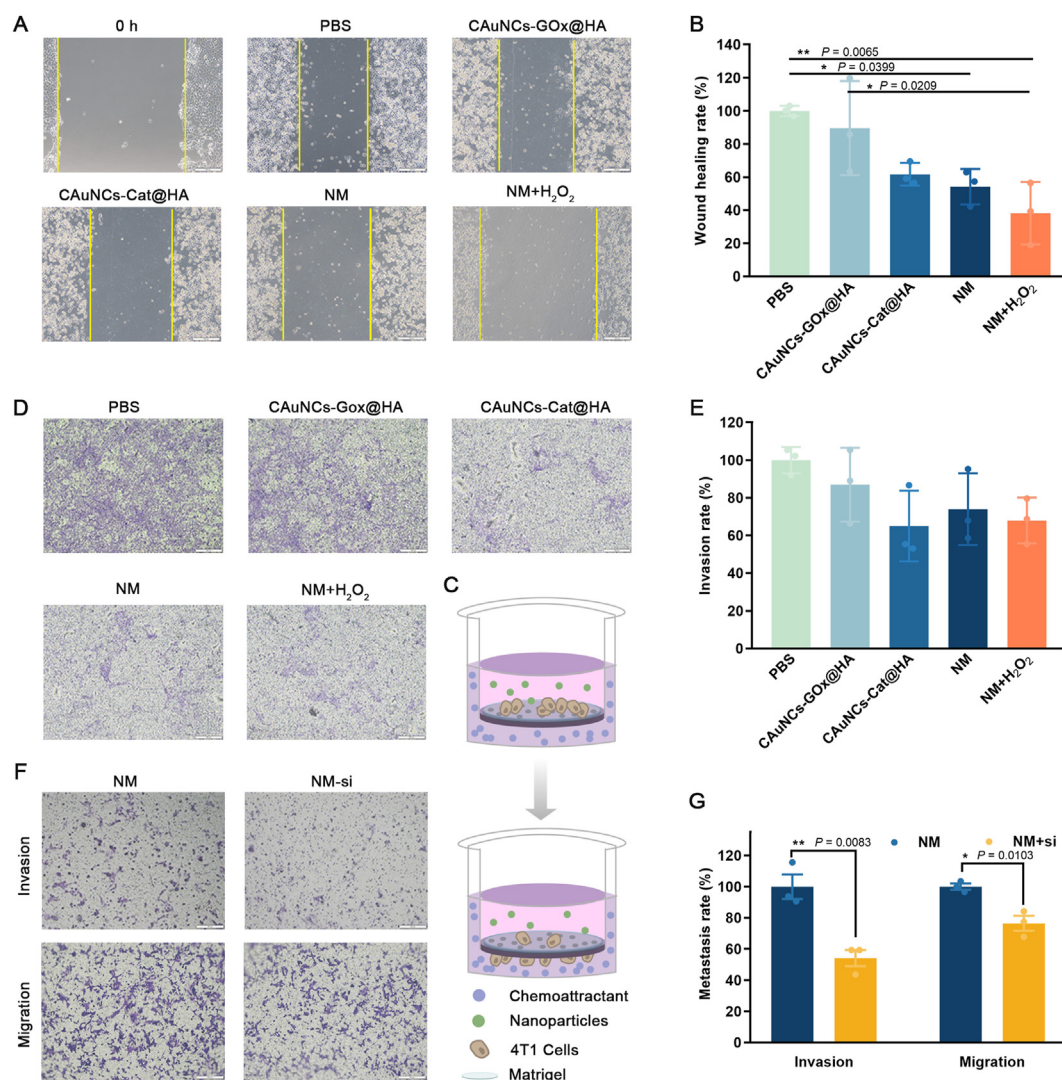
Figure 6 (A) Wound healing images and (B) healing rate of 4T1 cells after incubated with PBS, CAuNCs-GOx@HA, CAuNCs-Cat@HA, NM and NM + H_2O_2 for 24 h under hypoxia. (C) Schematic diagram of migration and invasion detection through transwell. (D) Images and (E) quantitative analysis of invaded 4T1 cells after different treatments under hypoxia. (F) Images and (G) quantitative analysis of migration and invasion ability of HK-2 silenced 4T1 cells. Data are presented as mean $\pm$ SD ($n = 3$), and one-way ANOVA with Tukey multiple comparisons post-test was used for (B) and (E). Two-tailed independent Student's t-test was used for (G); *$P < 0.05$, **$P < 0.01$, ***$P < 0.001$.

wound healing assay (Fig. 6A). The former scratching gap of PBS control group was narrowed significantly after 24 h incubation in hypoxia environment, demonstrating the strong wound healing ability of 4T1 cells. Cells treated with CAuNCs-GOx@HA also displayed a narrowed gap, and we speculated that might because of the consumption of oxygen during the glucose oxidation process, which made the hypoxia situation more severe. On contrast, with the combination of Cat, the cascade enzymatic reaction would alleviate the hypoxia, and the motility of 4T1 cells was inhibited in some way. The inhibition was further enhanced when H_2O_2 was given, and there was only a minor migration to the scratch. To make the migration differences more intuitive, we measured the scratch area by Image J for semi-quantification, and the wound healing rate of PBS group was considered as 100% (Fig. 6B). As shown, the wound healing rate of CAuNCs-GOx@HA and CAuNCs-Cat@HA was 89.63% and 61.71%, respectively, while it reduced to 54.21% with NM, and only 38.24% with NM + H_2O_2. Statistical analysis also showed that there was a significant difference between PBS and NM group,

PBS and NM + H_2O_2 group, as well as CAuNCs-GOx@HA and NM + H_2O_2 group.

The invasion motility and the ECM penetration ability of 4T1 cells were then evaluated, which utilized the Matrigel-coated transwells to simulate the actual microenvironment (Fig. 6C). The results exhibited the same trend as the wound healing assay (Fig. 6D and E). Majority of cells could invade across the Matrigel-coated membrane in PBS and CAuNCs-GOx@HA group, with the invasion rate of 86.96% after treatment with CAuNCs-GOx@HA. And the invasion rate further reduced to 73.96% and 67.97% of NM and NM + H_2O_2 group. Additionally, we noticed that after treatment with CAuNCs-Cat@HA, the invasion ability of 4T1 cells was strongly inhibited with the invasion rate of 65.10%, which was consistent with the previous immunofluorescence result of HIF-1α, demonstrating the relief of hypoxia could inhibit the invasion of 4T1 cells.

To further investigate the effect of HK-2 silencing on tumor migration and invasion. We delivered HK-2 siRNA via NM to
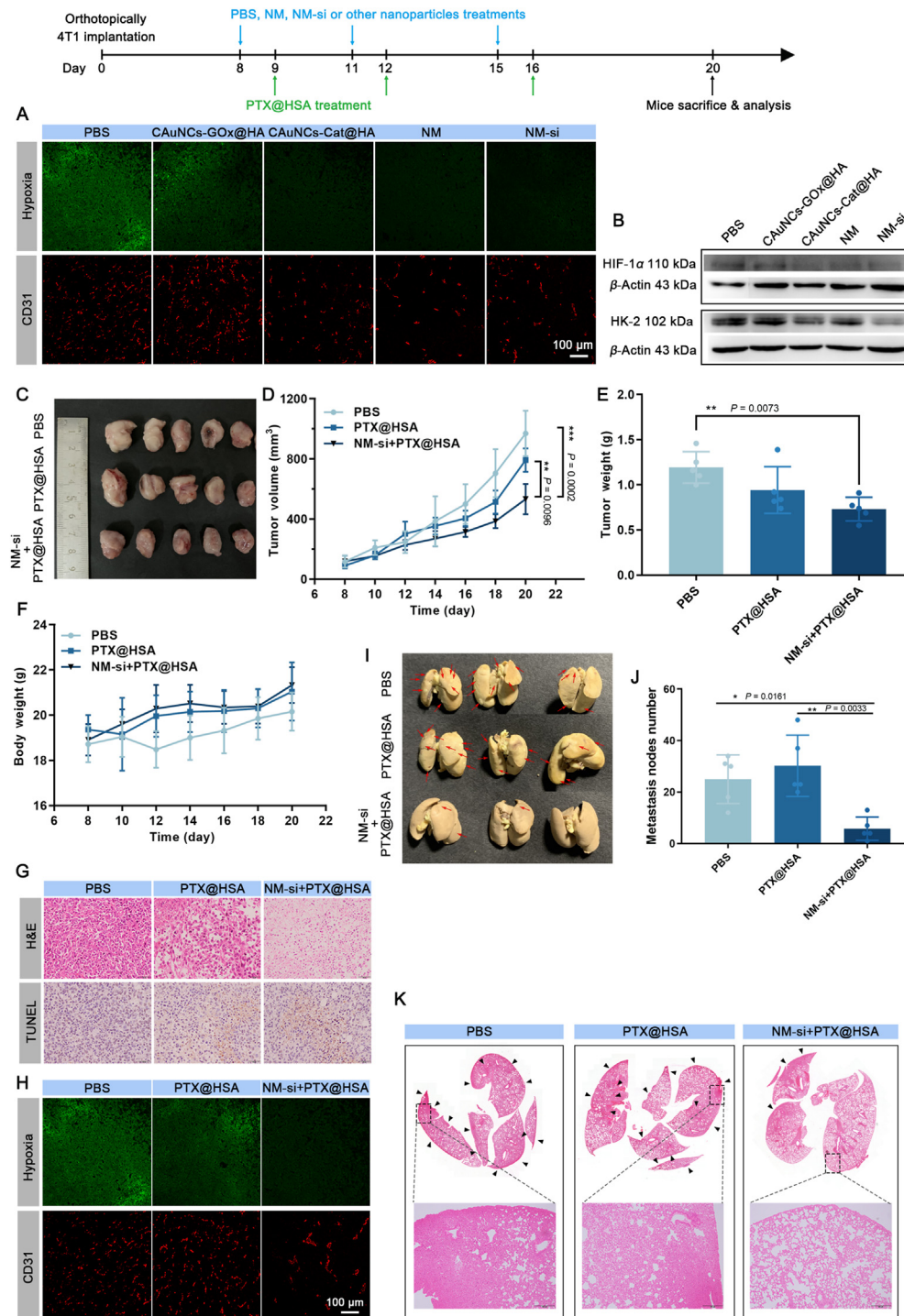
Figure 7   (A) Immunofluorescence images of tumor slices. Green represents hypoxia areas stained with anti-pimonidazole antibody and red represents blood vessels stained with anti-CD31 antibody. Scale bar = 100 μm. (B) Western blots of HIF-1α and HK-2 expression in tumors after different treatments. (C) Tumor images and tumor weights (E) at the end point after different treatments. (D) Tumor growth curves after different treatments ($n=5$). (F) Body weights of 4T1-tumor-bearing mice during the whole therapeutic process ($n = 5$). (G) H&E and TUNEL staining of tumor slices. (H) Tumor microenvironment modulation analysis of hypoxia and blood vessels through immunofluorescence images. Scale bar = 100 μm. (I) Representative *ex vivo* images of lungs and their (K) H&E staining. Metastasis nodules are indicated by red and black arrows respectively. (J) Number of metastasis nodules ($n = 5$). Data are presented as mean ± SD ($n = 5$), and one-way ANOVA with Tukey multiple comparisons post-test was used for analysis; *$P < 0.05$, **$P < 0.01$, and ***$P < 0.001$.

silence the protein, and 4T1 cells that only incubated with NM were set as negative control. Results demonstrate that RNA interference of HK-2 could extremely reduce the migration of 4T1 cells, and the inhibition effect was rather greater on invasion motility (Fig. 6F and G), which might be related to the decreased accumulation of lactic acid[23]. Moreover, the wound healing experiment even demonstrated that after knocking down the expression of HK-2, the capability of lateral migration was also greatly inhibited, with wound healing rate reduced to only 10.36% (Supporting Information Fig. S6).

3.10. Microenvironment modulation

Since the effective entry of NM into tumor was successfully verified, we continued to test the ability of NM with the loading of HK-2 siRNA for TME modulation *in vivo*. Here, the relief of hypoxia and inhibition of aerobic glycolysis *in vivo* were detected by immunofluorescence staining of tumor slices and Western blot (Fig. 7A). As shown, all the Cat-contained treatments (CAuNCs-Cat@HA, NM and NM-si) exhibited little hypoxia signal as compared to the strong hypoxia signal of PBS-treated group. The CD31 staining of tumor blood vessel demonstrated the same result. In hypoxia area (PBS- and CAuNCs-GOx@HA-treated group), high intensity and tortuous blood vessels were observed on account of the demand for more oxygen supply, while the intensity of blood vessels was significantly reduced after Cat was co-delivered, indicating that the cascade catalytic reaction between GOx and Cat could successfully alleviate tumor hypoxia. Western blot results further show that there was almost no expression of HIF-1α after co-loaded with Cat (Fig. 7B). Total protein of tumor was extracted to detect the expression of HK-2, and it suggested that the siRNA interference worked well in mice after treatment for three times. There was a significant knockdown of HK-2 protein after treated with NM-si when compared to PBS group. It was noteworthy that the expression of HK-2 in CAuNCs-Cat@HA exhibited a slightly reduction, and we deduced that might come from the decrease of HIF-1α which was also the upstream transcription factor of HK-2. Moreover, major organs were collected for H&E staining (Supporting Information Fig. S7), and no obvious histological difference was observed in all groups except CAuNCs-GOx@HA. Degeneration and necrosis of renal tubular epithelial cells were detected in CAuNCs-GOx@HA group, which might due to the toxic H_2O_2 produced by GOx during the glucose oxidation. However, the toxicity was greatly reduced after combination with Cat for H_2O_2 decomposition (group NM and NM-si).

3.11. In vivo anti-tumor and anti-metastasis efficacy

With the excellent ability of TME modulation, we further synergized NM-si with PTX@HSA to explore the anti-tumor and anti-metastasis efficacy. After treatments for three times, the 4T1-tumor-bearing mice were sacrificed and analyzed (Fig. 7C–E). As expected, mice treated with NM-si + PTX@HSA exhibited the slowest tumor growth during the treatment period, and there was a significant difference of tumor weights at the last day between PBS group and NM-si + PTX@HSA group. Moreover, no weight loss of mice was observed (Fig. 7F), indicating no systematic toxicity of NM-si. H&E and TUNEL staining of tumor slices were further performed to assess the anti-tumor effect (Fig. 7G). Prominent tumor tissue necrosis and apoptosis were observed in the synergy treatment (NM-si + PTX@HSA) when compared to

PBS and PTX@HSA group. And H&E staining of major organs showed negligible damage after the whole treatment (Fig. S7). Also, the microenvironment of tumor was evaluated, and as expected, the hypoxia was greatly relieved and aerobic glycolysis process was significantly inhibited (Fig. 7H and Supporting Information Fig. S8).

Further, lungs were collected and stained with Bouin's liquid to measure the metastasis inhibition (Fig. 7I and J). As shown, mice with only PBS treatment showed obvious lung metastasis with significant nodules displayed, while the synergistic treated mice showed negligible metastasis nodules. Interestingly, though there was no significant difference of tumor weights between PTX@HSA group and NM-si + PTX@HSA group, the metastasis nodules of NM-si + PTX@HSA are significantly less. H&E staining of lung slices demonstrated the same results (Fig. 7K). All these positive results illustrate that with the assistance of hypoxia alleviation and aerobic glycolysis inhibition, the lung metastasis of breast cancer could be successfully inhibited.

4. Conclusions

Summarily, we successfully synthesized the self-propelled nanomotor by utilizing the cascade catalytic reaction between GOx and Cat. The autonomous movement facilitated nanomotor with a faster speed and unique internalization mechanism. NM-si could be delivered to deep tumor and enter tumor cells without getting trapped in lysosomes. By utilizing the oxygen persistently generated from nanomotor and the siRNA interference technique to knockdown the key enzyme of glycolysis, NM-si exhibited extraordinary TME modulation ability both *in vitro* and *in vivo*, with significant hypoxia alleviation and aerobic glycolysis inhibition. After combined with PTX@HSA, promising anti-metastasis effect was demonstrated in 4T1-tumor bearing mice after pre-treated with NM-si for TME modulation. The reconstruction of TME through synergistic hypoxia alleviation and aerobic glycolysis inhibition shed light on a new strategy to prevent TNBC malignancy, and the cascade enzyme-powered NM-si exhibited as a potential nanoplatform for microenvironment modulation to inhibit breast cancer lung metastasis.

Author contributions

Huile Gao, Yi Qin and Wenqi Yu designed the research. Wenqi Yu, Ruyi Lin, Xueqin He, Xiaotong Yang and Huilin Zhang carried out the experiment. Wenqi Yu wrote mainly of the manuscript and Chuan Hu, Rui Liu, Huile Gao assisted with the manuscript reviewing. Yuan Huang, Yi Qin and Huile Gao provided the funding. All authors have given approval of the final version of the manuscript.

Conflicts of interest

The authors have no conflicts of interest to declare.

Appendix A.   Supporting Information

Supporting data to this article can be found online at https://doi.org/10.1016/j.apsb.2021.04.006.

References

1. Harbeck N, Gnant M. Breast cancer. *Lancet* 2017;**389**:1134−50.
2. Zhang W, Wang F, Hu C, Zhou Y, Gao HL, Hu J. The progress and perspective of nanoparticle-enabled tumor metastasis treatment. *Acta Pharm Sin B* 2020;**10**:2037−53.
3. Harris AL. Hypoxia—a key regulatory factor in tumour growth. *Nat Rev Cancer* 2002;**2**:38−47.
4. Zeng W, Liu PY, Pan WM, Singh SR, Wei YY. Hypoxia and hypoxia inducible factors in tumor metabolism. *Cancer Lett* 2015;**356**:263−7.
5. Zeng W, Wan R, Zheng YH, Singh SR, Wei YY. Hypoxia, stem cells and bone tumor. *Cancer Lett* 2011;**313**:129−36.
6. Folmes CD, Dzeja PP, Nelson TJ, Terzic A. Metabolic plasticity in stem cell homeostasis and differentiation. *Cell Stem Cell* 2012;**11**:596−606.
7. Jiang ZH, Liu ZX, Li MY, Chen C, Wang XS. Increased glycolysis correlates with elevated immune activity in tumor immune microenvironment. *EBioMedicine* 2019;**42**:431−42.
8. DeNardo DG, Ruffell B. Macrophages as regulators of tumour immunity and immunotherapy. *Nat Rev Immunol* 2019;**19**:369−82.
9. Hockel M, Vaupel P. Tumor hypoxia: definitions and current clinical, biologic, and molecular aspects. *J Natl Cancer Inst* 2001;**93**:266−76.
10. Yu WQ, Liu R, Zhou Y, Gao HL. Size-tunable strategies for a tumor targeted drug delivery system. *ACS Cent Sci* 2020;**6**:100−16.
11. Yu WQ, Shevtsov M, Chen XC, Gao HL. Advances in aggregatable nanoparticles for tumor-targeted drug delivery. *Chin Chem Lett* 2020;**31**:1366−74.
12. Ren JJ, Zhang L, Zhang JY, Zhang W, Cao Y, Xu ZG, et al. Light-activated oxygen self-supplied starving therapy in near-infrared (NIR) window and adjuvant hyperthermia-induced tumor ablation with an augmented sensitivity. *Biomaterials* 2020;**234**:119771.
13. Peng SJ, Liu JS, Qin Y, Wang H, Cao BL, Lu LG, et al. Metal-organic framework encapsulating hemoglobin as a high-stable and long-circulating oxygen carriers to treat hemorrhagic shock. *ACS Appl Mater Interfaces* 2019;**11**:35604−12.
14. Liu XL, Jansman MMT, Hosta-Rigau L. Haemoglobin-loaded metal organic framework-based nanoparticles camouflaged with a red blood cell membrane as potential oxygen delivery systems. *Biomater Sci* 2020;**8**:5859−73.
15. Reinišová L, Hermanová S, Pumera M. Micro/nanomachines: what is needed for them to become a real force in cancer therapy? *Nanoscale* 2019;**11**:6519−32.
16. Wang JJ, Dong RF, Wu HY, Cai YP, Ren BY. A review on artificial micro/nanomotors for cancer-targeted delivery, diagnosis, and therapy. *Nano-Micro Lett* 2019;**12**:11.
17. Lin RY, Yu WQ, Chen XC, Gao HL. Self-propelled micro/nanomotors for tumor targeting delivery and therapy. *Adv Healthc Mater* 2021;**10**:2001212.
18. You M, Chen CR, Xu LL, Mou FZ, Guan JG. Intelligent micro/nanomotors with taxis. *Acc Chem Res* 2018;**51**:3006−14.
19. Wang J, Manesh KM. Motion control at the nanoscale. *Small* 2010;**6**:338−45.
20. Joseph A, Contini C, Cecchin D, Nyberg S, Ruiz-Perez L, Gaitzsch J, et al. Chemotactic synthetic vesicles: design and applications in blood-brain barrier crossing. *Sci Adv* 2017;**3**:e1700362.
21. Kuang Y, Balakrishnan K, Gandhi V, Peng X. Hydrogen peroxide inducible DNA cross-linking agents: targeted anticancer prodrugs. *J Am Chem Soc* 2011;**133**:19278−81.
22. Koppenol WH, Bounds PL, Dang CV. Otto Warburg's contributions to current concepts of cancer metabolism. *Nat Rev Cancer* 2011;**11**:325−37.
23. Thews O, Riemann A. Tumor ph and metastasis: a malignant process beyond hypoxia. *Cancer Metastasis Rev* 2019;**38**:113−29.
24. Hirschhaeuser F, Sattler UG, Mueller-Klieser W. Lactate: a metabolic key player in cancer. *Cancer Res* 2011;**71**:6921−5.
25. Wolf A, Agnihotri S, Micallef J, Mukherjee J, Sabha N, Cairns R, et al. Hexokinase 2 is a key mediator of aerobic glycolysis and promotes tumor growth in human glioblastoma multiforme. *J Exp Med* 2011;**208**:313−26.
26. Li L, Kang L, Zhao W, Feng YY, Liu WP, Wang T, et al. Mir-30a-5p suppresses breast tumor growth and metastasis through inhibition of ldha-mediated warburg effect. *Cancer Lett* 2017;**400**:89−98.
27. Gao WW, de Avila BE, Zhang LF, Wang J. Targeting and isolation of cancer cells using micro/nanomotors. *Adv Drug Deliv Rev* 2018;**125**:94−101.
28. Yu WQ, He XQ, Yang ZH, Yang XT, Xiao W, Liu R, et al. Sequentially responsive biomimetic nanoparticles with optimal size in combination with checkpoint blockade for cascade synergetic treatment of breast cancer and lung metastasis. *Biomaterials* 2019;**217**:119309.
29. Liu R, Xiao W, Hu C, Xie R, Gao HL. Theranostic size-reducible and no donor conjugated gold nanocluster fabricated hyaluronic acid nanoparticle with optimal size for combinational treatment of breast cancer and lung metastasis. *J Control Release* 2018;**278**:127−39.
30. Frohlich E. The role of surface charge in cellular uptake and cytotoxicity of medical nanoparticles. *Int J Nanomedicine* 2012;**7**:5577−91.
31. Yu T, Malugin A, Ghandehari H. Impact of silica nanoparticle design on cellular toxicity and hemolytic activity. *ACS Nano* 2011;**5**:5717−28.
32. Luo ZJ, Dai Y, Gao HL. Development and application of hyaluronic acid in tumor targeting drug delivery. *Acta Pharm Sin B* 2019;**9**:1099−112.
33. Li HA, Sun ZY, Jiang SQ, Lai XY, Bockler A, Huang HH, et al. Tadpole-like unimolecular nanomotor with sub-100 nm size swims in a tumor microenvironment model. *Nano Lett* 2019;**19**:8749−57.
34. Sengupta S, Dey KK, Muddana HS, Tabouillot T, Ibele ME, Butler PJ, et al. Enzyme molecules as nanomotors. *J Am Chem Soc* 2013;**135**:1406−14.
35. Peng F, Tu Y, van Hest JC, Wilson DA. Self-guided supramolecular cargo-loaded nanomotors with chemotactic behavior towards cells. *Angew Chem Int Ed* 2015;**54**:11662−5.
36. Esteban-Fernandez de Avila B, Angell C, Soto F, Lopez-Ramirez MA, Baez DF, Xie SB, et al. Acoustically propelled nanomotors for intracellular sirna delivery. *ACS Nano* 2016;**10**:4997−5005.
37. Gao Y, Jia L, Wang Q, Hu HY, Zhao XL, Chen DW, et al. Ph/redox dual-responsive polyplex with effective endosomal escape for codelivery of sirna and doxorubicin against drug-resistant cancer cells. *ACS Appl Mater Interfaces* 2019;**11**:16296−310.